GTD-based Scattering Models for Bistatic SAR

Brian D. Rigling and Randolph L. Moses

The Ohio State University
Department of Electrical and Computer Engineering
2015 Neil Avenue, Columbus OH 43210-1272 USA

ABSTRACT

This paper discusses development of physics-based models for bistatic scattering. We generalize parametric equations for monostatic scattering mechanisms in a plane to achieve analogous bistatic approximations. Combination of these mechanisms, as separable azimuth and elevation components, allows 3-D modelling of six scattering primitives: sphere, tophat, trihedral, dihedral, cylinder, and flat plate. The responses of these scattering center models are shown to compare favorably with results obtained from validated high-frequency simulations.

Keywords: SAR, bistatic, ground map, scattering models, Geometric Theory of Diffraction.

1. INTRODUCTION

Synthetic aperture radar (SAR) is an invaluable tool in all-weather air-to-ground surveillance. Monostatic SAR systems, which involve a single platform operating as transmitter and receiver, are historically cost effective, straightforward to implement, and easy to deploy operationally. However, recent advancements in unmanned aerial vehicle technology, as well as growing interest in both stealth and cooperative surveillance, have introduced new interest in the field of bistatic SAR Ref. 1–3.

In bistatic Ref. 4 systems, the transmit and receive antennas are located on separate platforms. The receiver may be of relatively low cost, and its passive nature allows it to safely operate at closer ranges to hostile territory. One or more receivers may work cooperatively with a higher cost transmitting platform at a safe standoff distance, or may make use of illuminators of opportunity such as local television and radio transmitters or even overpassing satellites Ref. 5.

According to the geometric theory of diffraction (GTD) Ref. 6, the high-frequency scattering response from a complex object is well-modelled by the sum of responses from individual scattering mechanisms. GTD-based parametric models for monostatic SAR scatterers provide a physically relevant representation of an object's scattering behavior, and thus are potentially valuable tools for SAR image exploitation. Reliable feature extraction may provide for image chip compression Ref. 7 and may serve as input to automatic target recognition (ATR) processors. The authors of Ref. 8–12 propose attributed scattering center models for monostatic returns from several canonical reflectors, including trihedrals, dihedrals, and tophats. These models have given promising results when applied in ATR algorithms Ref. 8, 13–16. These algorithms operate by parametrically extracting target features which then go on to feed Bayes-classification engines. Canonical scattering center models could be similarly effective in bistatic SAR ATR.

As compared to the monostatic scattering community, there exists relatively little work in the open literature regarding application of scattering center models to bistatic SAR imagery. Gabig Ref. 17 attempts to experimentally validate monostatic to bistatic equivalence theorems, which have been proposed by many researchers Ref. 18–20. Equivalence theorems principally apply monostatic models to bistatic scattering by using the bistatic look angle in place of the monostatic look angle. These theorems are typically more concerned with the total radar cross section of a complex target, rather than the returns of individual scatterers. Germond Ref. 21 derives expressions for bistatic radar polarimetry from the classical monostatic theory. Akhter Ref. 22 develops several electromagnetic models for bistatic scattering based on the geometric theory of diffraction. In this paper, we

Corresponding author's address: Brian D. Rigling, 5649-301 Columbia Rd, Columbia, MD 21044, E-mail: (brigling@earthlink.net).

Algorithms for Synthetic Aperture Radar Imagery XI, edited by Edmund G. Zelnio, Frederick D. Garber, Proceedings of SPIE Vol. 5427 (SPIE, Bellingham, WA, 2004)
0277-786X/04/$15 · doi: 10.1117/12.541555

use the theory demonstrated in Ref. 22, and generalize the models found in Ref. 8, 11, 12, to develop parsimonious physics-based models of bistatic scattering. The need to consider differing transmitter and receiver aspect angles in the bistatic geometry necessarily adds to the complexity of the models, but intuitive modification of monostatic formulas may sufficiently bridge the gaps in bistatic scattering theory left by the electromagnetics community. To demonstrate application of this theory, we examine the inverse scattering problem of estimating the parameters of scattering centers based on a synthetically-generated bistatic SAR image.

The remainder of this paper is organized as follows. Section II describes the process of bistatic SAR data collection and image formation formation via matched filtering. Section III introduces three models for fundamental bistatic scattering mechanisms in a plane. Section IV shows how various combinations of these models may be used to approximate the scattering behavior of six three-dimensional scattering primitives: trihedral, tophat, sphere, dihedral, cylinder and plate. Lastly, Section VI summarizes our results and conclusions.

2. BISTATIC SAR

Consider the bistatic SAR geometry in Figure 1. A transmitter following a path $\underline{r}_t(\tau)$, where τ is time, interrogates a region centered at the origin. A receiver following a path $\underline{r}_r(\tau)$ measures backscattered energy from the region. The slant ranges of the transmitter and receiver are $R_t(\tau) = \|\underline{r}_t(\tau)\|$ and $R_r(\tau) = \|\underline{r}_r(\tau)\|$, respectively, and $\phi_t(\tau)$ and $\phi_r(\tau)$ ($\theta_t(\tau)$ and $\theta_r(\tau)$) are the azimuth (elevation) angles of the transmitter and receiver at time τ. Given these values, the transmitter location at a given time τ is

$$\begin{aligned} \underline{r}_t(\tau) &= [x_t(\tau) \quad y_t(\tau) \quad z_t(\tau)]^T \\ &= R_t(\tau)[\cos\phi_t(\tau)\cos\theta_t(\tau) \quad \sin\phi_t(\tau)\cos\theta_t(\tau) \quad \sin\theta_t(\tau)]^T, \end{aligned} \tag{1}$$

and the receiver location is

$$\begin{aligned} \underline{r}_r(\tau) &= [x_r(\tau) \quad y_r(\tau) \quad z_r(\tau)]^T \\ &= R_r(\tau)[\cos\phi_r(\tau)\cos\theta_r(\tau) \quad \sin\phi_r(\tau)\cos\theta_r(\tau) \quad \sin\theta_r(\tau)]^T. \end{aligned} \tag{2}$$

Measurements of the transmitter and receiver positions are subject to error, and these errors introduce slow time dependent phase errors in the recorded data Ref. 23. Provided that the severity of these measurement errors is limited, they may be corrected to within a linear phase term by post-processing techniques. For the remainder of our discussion, we assume that all of the motion measurement errors in the system are strictly within our ability to correct with autofocus algorithms Ref. 23–25.

At regular intervals during the data collection period $\tau \in [-T/2, T/2]$, the transmitting platform spotlights the scene of interest with radiated energy. The projected energy is assumed to have uniform power over the frequency range $f \in [f_0, f_0 + B]$ and to have uniform power over the projected beam. The receiving platform records the reflected responses without introducing any spectral distortions. High-frequency approximations Ref. 6 allow the composite response from the scene to be modelled as the sum of responses from individual scatters. Thus, we represent the returned signal as

$$S(f,\tau) = \sum_m A_m S_{\Gamma(m)}(f, \phi_t(\tau), \phi_r(\tau), \theta_t(\tau), \theta_r(\tau); \underline{\theta}^{(m)}) e^{-j\frac{2\pi f}{c}\Delta R_m(\tau)} + w(f,\tau) \tag{3}$$

where the response of the mth reflector in the scene is $S_{\Gamma(m)}(f, \phi_t, \phi_r, \theta_t, \theta_r; \underline{\theta}^{(m)})$. The variable $\Gamma(m)$ indicates the type of canonical scattering center, and therefore the equational form of $S_{\Gamma(m)}(f, \phi_t, \phi_r, \theta_t, \theta_r; \underline{\theta}^{(m)})$. In Section IV, we propose six types of canonical scatterers such that $\Gamma(m) \in \{$sphere, tophat, trihedral, dihedral, cylinder, plate$\}$. The vector $\underline{\theta}^{(m)}$ contains the physical parameters corresponding to a reflector of type $\Gamma(m)$. The return from each scatterer is time-delayed by the travel time from the transmitter to the scatterer to the receiver. The receiver gates the recorded data at each point of observation such that scatterers at the origin have zero time delay. In (3), $\Delta R_m(\tau)/c$ is the time delay of the mth scatterer relative to the time delay of a scatterer located at the origin, and A_m is the reflector's real-valued scattering coefficient. The speed of light is represented by c, and $w(f,\tau)$ is white Gaussian measurement noise.

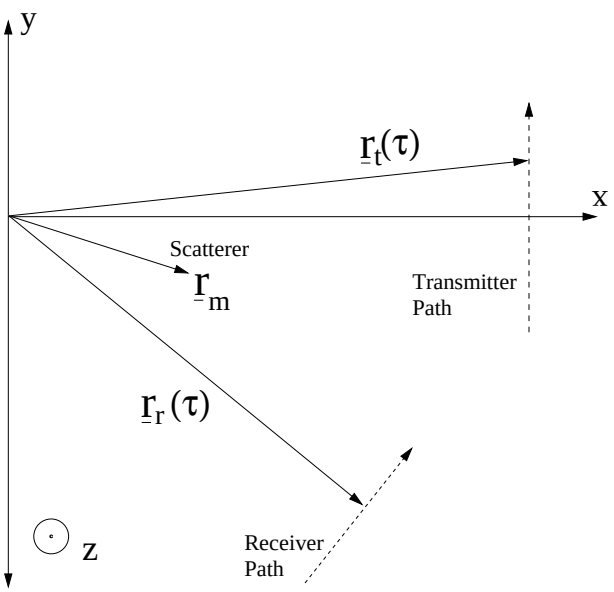

Figure 1. Top view of a bistatic data collection geometry. The x-y plane is the ground plane.

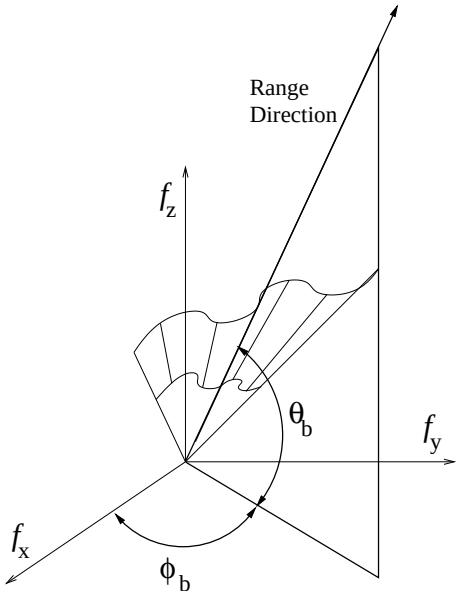

Figure 2. Bistatic SAR data collection manifold in 3-D frequency space.

Assuming that the imaged scene is small relative to the platform ranges allows a far-field assumption to be used to approximate the differential range $\Delta R_m(\tau)$ Ref. 26, giving

$$\begin{aligned}\Delta R_m(\tau) \quad \approx \quad & -x_m \left(\cos\phi_t(\tau)\cos\theta_t(\tau) + \cos\phi_r(\tau)\cos\theta_r(\tau)\right) \\ & -y_m \left(\sin\phi_t(\tau)\cos\theta_t(\tau) + \sin\phi_r(\tau)\cos\theta_r(\tau)\right) \\ & -z_m \left(\sin\theta_t(\tau) + \sin\theta_r(\tau)\right). \end{aligned} \tag{4}$$

Using equation (4), our expression for the recorded data (3) becomes

$$S(f,\tau) \approx \sum_m A_m S_{\Gamma(m)}(f_x, f_y, f_z; \underline{\theta}^{(m)}) e^{j\frac{4\pi}{c}(x_m f_x(f,\tau) + y_m f_y(f,\tau) + z_m f_z(f,\tau))} + w(f,\tau) \tag{5}$$

where

$$\begin{aligned} f_x(f,\tau) &= \frac{f}{2}\left(\cos\phi_t(\tau)\cos\theta_t(\tau) + \cos\phi_r(\tau)\cos\theta_r(\tau)\right) \\ f_y(f,\tau) &= \frac{f}{2}\left(\sin\phi_t(\tau)\cos\theta_t(\tau) + \sin\phi_r(\tau)\cos\theta_r(\tau)\right) \\ f_z(f,\tau) &= \frac{f}{2}\left(\sin\theta_t(\tau) + \sin\theta_r(\tau)\right). \end{aligned} \tag{6}$$

The data collection manifold is thus defined in frequency space as the surface of points $\{(f_x(f,\tau), f_y(f,\tau), f_z(f,\tau))\}$ for $f \in [f_0, f_0 + B]$ and $\tau \in [-T/2, T/2]$, as shown in Figure 2. This manifold may also be viewed as the surface swept out by the bistatic line-of-sight, written in vector form as

$$\underline{v}_{LOS}(\tau) = \frac{1}{2}\begin{bmatrix} \cos\phi_t(\tau)\cos\theta_t(\tau) + \cos\phi_r(\tau)\cos\theta_r(\tau) \\ \sin\phi_t(\tau)\cos\theta_t(\tau) + \sin\phi_r(\tau)\cos\theta_r(\tau) \\ \sin\theta_t(\tau) + \sin\theta_r(\tau) \end{bmatrix}. \tag{7}$$

Given a set of bistatic SAR phase history data $\{S(f,\tau)\}$ for $f \in [f_0, f_0 + B]$ and $\tau \in [-T/2, T/2]$, one typically wishes to form an image defined by a uniformly spaced grid of sample points, or pixels, on a plane. By analyzing

one pixel at a time, one may assume that a point scatterer (*i.e.*, $S_{\Gamma(m)}(f, \phi_t, \phi_r, \theta_t, \theta_r; \underline{\theta}^{(m)}) \equiv 1$) is located at each pixel's grid location. Then, the value of that pixel is computed as the maximum likelihood estimate of the complex reflection coefficient $P(x, y, z)$ at that location, from the measurements $\{S(f, \tau)\}$. Maximum likelihood estimation of $P(x, y, z)$ under the assumption of white Gaussian measurement errors in the phase history data requires minimization of a least squares cost function written as

$$J_P = \sum_{i=1}^{N_f} \sum_{k=1}^{N_\tau} \left| S(f_i, \tau_k) - P(x, y, z) e^{j \frac{4\pi}{c}(x f_x(f_i,\tau_k) + y f_y(f_i,\tau_k) + z f_z(f_i,\tau_k))} \right|^2. \tag{8}$$

Differentiating the cost function J with respect to the real and imaginary parts of $P(x, y, z)$, and setting the result equal to zero, allows one to solve for the least squares estimate of the pixel value, expressed as

$$P(x, y, z) = \frac{1}{N_f N_\tau} \sum_{i=1}^{N_f} \sum_{k=1}^{N_\tau} S(f_i, \tau_k) e^{-j \frac{4\pi}{c}(x f_x(f_i,\tau_k) + y f_y(f_i,\tau_k) + z f_z(f_i,\tau_k))}. \tag{9}$$

Equation (9) gives the matched filtering image formation algorithm Ref. 26 for each image pixel with location (x, y, z).

3. PLANAR BISTATIC SCATTERING MECHANISMS

We now introduce three fundamental mechanisms for scattering in a plane. In planar scattering models, the extents of a reflector out of the plane are assumed to be electrically large Ref. 22 (*i.e.*, greater than λ), such that the third dimension need not be considered. Combinations of these mechanisms can effectively model the principal components of several canonical scattering centers in three dimensions. These models take a separable form where fundamental scattering mechanisms are used to approximate the azimuthal and elevational responses of canonical reflectors. However, the planar nature of bistatic SAR data collection will make capturing the principal behaviors of a reflector in each angular direction sufficient for most applications.

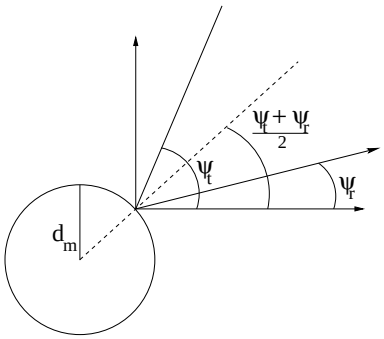

Figure 3. Circular scattering mechanism has an isotropic response that migrates around the surface as the look angle changes.

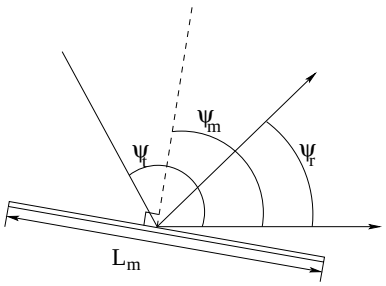

Figure 4. Flat scattering mechanism has an anisotropic response that peaks when the specular reflection is observed by the receiver.

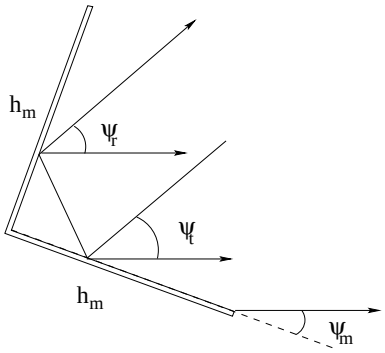

Figure 5. Right angle scattering mechanism has an anisotropic response that peaks when the transmitter and receiver are at the same aspect angle.

3.1. Circular

Figure 3 shows scattering from a circular surface. The circular mechanism has a response that is isotropic over all look angles $\psi_t, \psi_r \in [-\pi, \pi]$, and that is uniform over all frequencies $f \in [f_0, f_0 + B]$. Thus, we model its bistatic response as

$$S_{circ}(f, \psi_t, \psi_r) = 1. \tag{10}$$

The location of the response does migrate along the surface of the reflector as the bistatic look angle $\psi_b = (\psi_t + \psi_r)/2$ changes, such that the actual point of reflection is $(x, y) = (d_m \cos\psi_b, d_m \sin\psi_b)$ where d_m is the radius of curvature. However, in narrowband bistatic SAR, this migration is typically negligible because of the small angular span of the data collection. We can demonstrate this by considering the drift observed as a function of crossrange image resolution. In Ref. 26, crossrange resolution is shown to be approximately

$$\rho_y = \frac{c}{4f_0 \sin\left(\frac{\Delta\psi_b}{2}\right)} \tag{11}$$

where $\Delta\psi_b$ is the angular span swept through by the bistatic look angle ψ_b during data collection. Accordingly, the crossrange migration of the reflection point is

$$\Delta_y = 2d_m \sin\left(\frac{\Delta\psi_b}{2}\right). \tag{12}$$

Requiring this migration to be less than the width of a resolution cell gives

$$d_m < \frac{2\rho_y^2}{\lambda}, \quad \lambda = \frac{c}{f_0}. \tag{13}$$

For a SAR system operating at $f_0 = 10$ GHz, this limits the radius of curvature to 20 feet at 1-foot resolution but limits it to 7 inches at 2-inch resolution. Thus, the effect of a migrating reflection point may become significant in high-resolution or wide angle applications, which require data to be collected over a larger annular segment.

3.2. Flat Plate

Figure 4 shows scattering from a flat surface with length L_m and pose angle ψ_m, indicating the direction of the surface normal with respect to the x-axis. The planar model for monostatic scattering from a flat surface is Ref. 8, 11

$$S(f, \psi_t; L_m, \psi_m) = \left(j\frac{f}{f_c}\right)^{1/2} \operatorname{sinc}\left(\frac{2\pi f}{c} L_m \sin(\psi_t - \psi_m)\right), \quad \psi_t \in \left[\psi_m - \frac{\pi}{2}, \psi_m + \frac{\pi}{2}\right], \tag{14}$$

which may also be written as

$$S(f, \psi_t; L_m, \psi_m) = \left(j\frac{f}{f_c}\right)^{1/2} \frac{e^{j\frac{4\pi f}{c}\left(\frac{L_m}{2}\sin(\psi_t - \psi_m)\right)} - e^{-j\frac{4\pi f}{c}\left(\frac{L_m}{2}\sin(\psi_t - \psi_m)\right)}}{\frac{2\pi f}{c} L_m \sin(\psi_t - \psi_m)}, \quad \psi_t \in \left[\psi_m - \frac{\pi}{2}, \psi_m + \frac{\pi}{2}\right]. \tag{15}$$

One may view the numerator of (15) as the sum of the responses from two point scatterers, one located at each end of the flat surface. Therefore, to accomodate bistatic scattering behavior, we modify (15) to represent the sum of the bistatic returns from two point reflectors, written as

$$\begin{aligned} S_{flat}(f, \psi_t, \psi_r; L_m, \psi_m) &= \left(j\frac{f}{f_c}\right)^{1/2} \frac{e^{\frac{2\pi f}{c}\frac{L_m}{2}(\sin(\psi_t - \psi_m) + \sin(\psi_r - \psi_m))} - e^{-\frac{2\pi f}{c}\frac{L_m}{2}(\sin(\psi_t - \psi_m) + \sin(\psi_r - \psi_m))}}{\frac{\pi f}{c} L_m \left(\sin(\psi_t - \psi_m) + \sin(\psi_r - \psi_m)\right)}, \\ &\quad \psi_t, \psi_r \in \left[\psi_m - \frac{\pi}{2}, \psi_m + \frac{\pi}{2}\right], \end{aligned} \tag{16}$$

or equivalently

$$\begin{aligned} S_{flat}(f, \psi_t, \psi_r; L_m, \psi_m) &= \left(j\frac{f}{f_c}\right)^{1/2} \operatorname{sinc}\left(\frac{\pi f}{c} L_m (\sin(\psi_t - \psi_m) + \sin(\psi_r - \psi_m))\right), \\ &\quad \psi_t, \psi_r \in \left[\psi_m - \frac{\pi}{2}, \psi_m + \frac{\pi}{2}\right]. \end{aligned} \tag{17}$$

Note that (17) achieves its peak response when the receiver observes the specular reflection from the flat surface (*i.e.*, when $\psi_t - \psi_m = \psi_m - \psi_r$).

3.3. Right Angle

Figure 5 shows scattering from a right angle reflector, with sides of equal length h_m. The variable ψ_m indicates the angle measured counter-clockwise from the positive x-axis (so $\psi_m > 0$ in the figure). In Ref. 22, it is shown that the dominant bistatic response of a right angle reflection is given by

$$\begin{aligned} S_{right}(f,\psi_t,\psi_r;h_m,\psi_m) &= \left(j\frac{f}{f_c}\right)^{1/2} \sin\left(\frac{\psi_t+\psi_r-2\psi_m}{2}\right)\cdot \\ &\quad \operatorname{sinc}\left[\frac{4\pi f h_m}{c}\sin\left(\frac{\psi_t+\psi_r-2\psi_m}{2}\right)\sin\left(\frac{\psi_t-\psi_r}{2}\right)\right] \\ &\quad \psi_t,\psi_r \in \left[\psi_m-\frac{\pi}{4},\psi_m+\frac{\pi}{4}\right] \end{aligned} \tag{18}$$

provided $\psi_t - \psi_r$ is small. The peak response of (18) is observed when the transmitter and receiver are at the same aspect angle (*i.e.*, $\psi_t = \psi_r$).

4. CANONICAL SCATTERING CENTER MODELS

Combinations of the scattering mechanisms described in the previous section may effectively model the responses of three-dimensional scattering primitives. The basic circular, flat, and right angle responses approximate the azimuthal and elevational responses of each of the canonical scatterers shown in Table 1. Thus, the product of the approximate elevation and azimuth responses simulate the 3-D response of a scattering primitive. To simplify the notation and intuition of the resulting formulas, we define the bistatic look angles in azimuth ϕ_b and elevation θ_b as

$$\phi_b = \frac{\phi_t+\phi_r}{2} \quad \text{and} \quad \theta_b = \frac{\theta_t+\theta_r}{2}. \tag{19}$$

Similarly, the bistatic angles in azimuth β_ϕ and in elevation β_θ are

$$\beta_\phi = \phi_t - \phi_r \quad \text{and} \quad \beta_\theta = \theta_t - \theta_r. \tag{20}$$

We now explicitly consider each of the primitives shown in Table 1. In the following, we set the azimuth and elevation pose angles, ϕ_m and θ_m, to zero. At the end of this section, we show how the response of rotated scattering centers may be computed by implementing yaw, pitch, and roll transformations. Where appropriate, we verify our models by fitting curves to Xpatchf Ref. 27 predictions of a scatterer's radar cross section (RCS).

Table 1. Canonical scattering primitives.

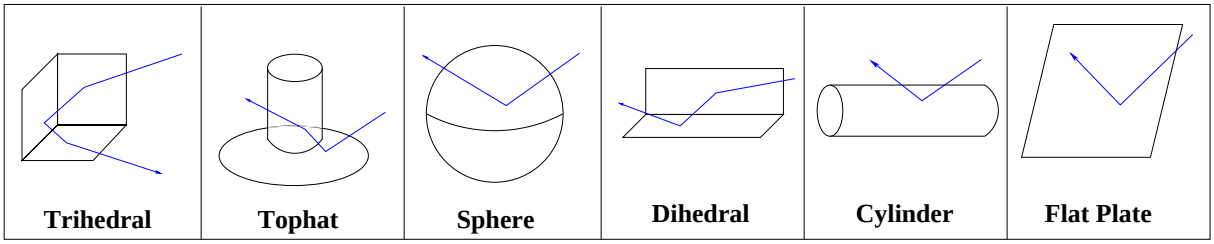

4.1. Sphere

A sphere is composed of circular surfaces in both azimuth and elevation, giving it a symmetric and uniform response from all aspect angles. This implies an RCS model of the form

$$S_{sph}(f,\phi_t,\phi_r,\theta_t,\theta_r) = S_{circ}(f,\phi_t,\phi_r)S_{circ}(f,\theta_t,\theta_r) = 1. \tag{21}$$

The only observable variation in a sphere's response, as a function of look angle, is the location of the point of reflection, which migrates around the surface of the sphere as a function of the transmitter (ϕ_t, θ_t) and receiver (ϕ_r, θ_r) aspect angles. The point of reflection is positioned on the surface of the sphere at the point corresponding to the bistatic look angle in azimuth ϕ_b and in elevation θ_b. As mentioned earlier, in narrowband systems that involve small angular spans in their data collections, the reflection point migration can often be neglected. Toward the goal of simple, parsimonious modelling, we thus neglect this location migration.

4.2. Tophat

The surface of a tophat is a circular mechanism in azimuth, making its response uniform with respect to the azimuth angles of the transmitter and receiver, but is a right angle mechanism in elevation, making its elevational response highly sensitive to any difference between the elevation angles of the transmitter and receiver. We model the scattering behavior of the tophat as

$$\begin{aligned} S_{top}(f,\phi_t,\phi_r,\theta_t,\theta_r;h_m) &= S_{circ}(f,\phi_t,\phi_r)S_{right}(f,\theta_t,\theta_r;h_m,\theta_m=0) \\ &= \left(j\frac{f}{f_c}\right)^{1/2}\sin\left(\frac{\theta_t+\theta_r}{2}\right)\cdot\mathrm{sinc}\left[\frac{4\pi f h_m}{c}\sin\left(\frac{\theta_t+\theta_r}{2}\right)\sin\left(\frac{\theta_t-\theta_r}{2}\right)\right], \\ &\quad \theta_t,\theta_r\in\left[0,\frac{\pi}{2}\right] \\ &= \left(j\frac{f}{f_c}\right)^{1/2}\sin\theta_b\mathrm{sinc}\left[\frac{4\pi f h_m}{c}\sin\theta_b\sin\left(\frac{\beta_\theta}{2}\right)\right], \\ &\quad \theta_t,\theta_r\in\left[0,\frac{\pi}{2}\right] \end{aligned} \tag{22}$$

where h_m is the height of the tophat.

Figure 8 compares the Xpatchf simulated RCS of a tophat to the modelled RCS, at $f = 9.5$ GHz. The tophat has a height of $h_m = 5$ meters, a base radius of 7 meters, and cylinder radius of 2 meters. The transmitter elevation angle is $\theta_t = 20°$, and the receiver elevation angle is varied from $\theta_r = 0°$ to $\theta_r = 90°$. Equation (22) predicts the angle and width of the peak RCS with reasonable accuracy, as shown in Figure 8. However, the side lobes of the tophat RCS are not well modelled below -15dB. This can be attributed to the fact that equation (18) is based on scattering from a dihedral with rectangular edges, which may give significantly different RCS variation than the circular edges of a tophat, and more importantly, (18) is derived by assuming β_θ to be small.

4.3. Trihedral

A trihedral scattering primitive has right angle scattering mechanisms in both azimuth and elevation. We model the response of a trihedral reflector as

$$\begin{aligned} S_{tri}(f,\phi_t,\phi_r,\theta_t,\theta_r;h_m) &= S_{right}(f,\phi_t,\phi_r;h_m,\phi_m=0)S_{right}(f,\theta_t,\theta_r;h_m,\theta_m=0) \\ &= \left(j\frac{f}{f_c}\right)\sin\left(\frac{\phi_t+\phi_r}{2}\right)\cdot\mathrm{sinc}\left[\frac{4\pi f h_m}{c}\sin\left(\frac{\phi_t+\phi_r}{2}\right)\sin\left(\frac{\phi_t-\phi_r}{2}\right)\right]\cdot \\ &\quad \sin\left(\frac{\theta_t+\theta_r}{2}\right)\cdot\mathrm{sinc}\left[\frac{4\pi f h_m}{c}\sin\left(\frac{\theta_t+\theta_r}{2}\right)\sin\left(\frac{\theta_t-\theta_r}{2}\right)\right] \\ &= \left(j\frac{f}{f_c}\right)\sin\phi_b\mathrm{sinc}\left[\frac{4\pi f h_m}{c}\sin\phi_b\sin\left(\frac{\beta_\phi}{2}\right)\right]\cdot \\ &\quad \sin\theta_b\mathrm{sinc}\left[\frac{4\pi f h_m}{c}\sin\theta_b\sin\left(\frac{\beta_\theta}{2}\right)\right],\ \theta_t,\theta_r\in\left[0,\frac{\pi}{2}\right],\ \phi_t,\phi_r\in\left[0,\frac{\pi}{2}\right] \end{aligned} \tag{23}$$

where the length of the trihedral along each edge is assumed to be equal to h_m.

Figures 6 and 7 compare the Xpatchf simulated RCS of a trihedral to the modelled RCS, at $f = 10$ GHz. The trihedral has height, width, and depth all defined to be $h_m = 2$ meters. In each, the transmitter aspect is constant at $(\phi_t, \theta_t) = (-30°, 30°)$. In Figure 6, the receiver azimuth angle varies from $\phi_r = -90°$ to $\phi_r = 0°$, and

in Figure 7, the receiver elevation angle varies from $\theta_r = 0°$ to $\theta_r = 90°$. In both figures, equation (23) accurately predicts the angle and width of the peak RCS. In Figure 6, the principal side lobe roll-off behavior is reasonably modelled, but in Figure 7, the elevational side lobes are not as well matched. Similar to the tophat model, this can be attributed to the fact that equation (18) is based on scattering from a dihedral with rectangular sides, which is more respresentative of a trihedral in azimuth than in elevation, and again, (18) requires β_ϕ and β_θ to be small.

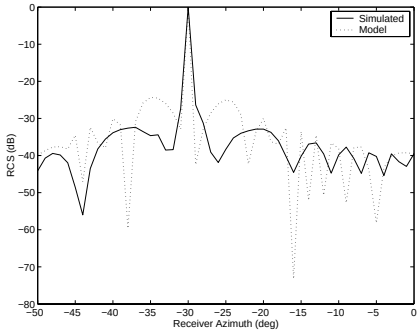

Figure 6. RCS of a trihedral as a function of receiver azimuth angle. The transmitter aspect angles are $(\phi_t, \theta_t) = (-30°, 30°)$.

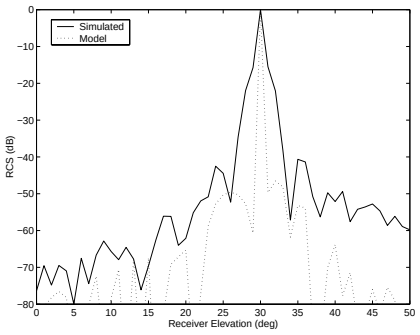

Figure 7. RCS of a trihedral as a function of receiver elevation angle. The transmitter aspect angles are $(\phi_t, \theta_t) = (-30°, 30°)$.

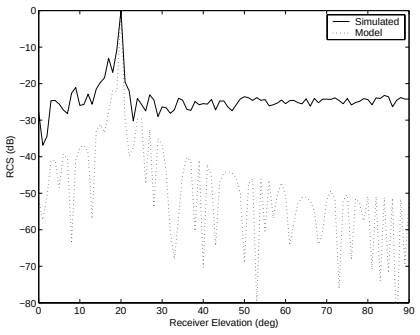

Figure 8. RCS of a tophat as a function of receiver elevation angle. The transmitter elevation angle is $\theta_t = 20°$.

4.4. Dihedral

A dihedral consists of a flat scattering mechanism in azimuth and a right angle scattering mechanism in elevation. We model the response of a dihedral reflector as

$$\begin{aligned} S_{dih}(f, \phi_t, \phi_r, \theta_t, \theta_r; L_m, h_m) &= S_{flat}(f, \phi_t, \phi_r; L_m, \phi_m = 0) S_{right}(f, \theta_t, \theta_r; h_m, \theta_m = 0) \\ &= \left(j\frac{f}{f_c}\right) \mathrm{sinc}\left(\frac{\pi f}{c} L_m (\sin\phi_t \cos\theta_t + \sin\phi_r \cos\theta_r)\right) \cdot \\ &\quad \sin\left(\frac{\theta_t + \theta_r}{2}\right) \cdot \mathrm{sinc}\left[\frac{4\pi f h_m}{c} \sin\left(\frac{\theta_t + \theta_r}{2}\right) \sin\left(\frac{\theta_t - \theta_r}{2}\right)\right] \\ &= \left(j\frac{f}{f_c}\right) \mathrm{sinc}\left(\frac{2\pi f_y L_m}{c}\right) \cdot \sin\theta_b \mathrm{sinc}\left[\frac{4\pi f h_m}{c} \sin\theta_b \sin\left(\frac{\beta_\theta}{2}\right)\right] \\ &\quad \theta_t, \theta_r \in \left[0, \frac{\pi}{2}\right], \quad \phi_t, \phi_r \in \left[-\frac{\pi}{2}, \frac{\pi}{2}\right] \end{aligned} \tag{24}$$

where L_m is the length of the dihedral, and h_m is equal to the height and depth of its sides. Note that we have modified the flat scattering mechanism by multiplying $\sin\phi_t$ with $\cos\theta_t$ and by multiplying $\sin\phi_r$ with $\cos\theta_r$. This adaptation is necessary to allow for the convergence of lines of longitude (corresponding to angles in azimuth) as elevation angles approach $\pm 90°$.

Figures 9, 10, and 11 compare the Xpatchf simulated RCS of a dihedral to the modelled RCS, at $f = 10$ GHz. The dihedral has length $L_m = 5$ meters and has height and depth $h_m = 2$ meters. In Figures 9 and 11, the transmitter aspect is constant at $(\phi_t, \theta_t) = (0°, 10°)$, and in Figure 10, the tranmitter aspect is $(\phi_t, \theta_t) = (30°, 10°)$. The receiver azimuth angle varies from $\phi_r = -30°$ to $\phi_r = 30°$ in Figures 9 and 10. In Figure 11, the receiver elevation angle varies from $\theta_r = 0°$ to $\theta_r = 90°$. In Figure 9, equation (24) is shown to be most accurate in predicting the peak and side lobe responses of the dihedral, when the transmitting aspect is parallel to the dihedral normal. In Figure 10, (24) accurately models in azimuth the principal side lobe behavior, and the modelled peak width and location match the simulation. Figure 11 shows that equation (24) accurately places the peak response in elevation and captures the principal side lobe behavior. From these figures, it is apparent

that the accuracy of our models breaks down as β_ϕ and β_θ become large and as the platform azimuth angles move away from $\phi_t = \phi_r = 0°$.

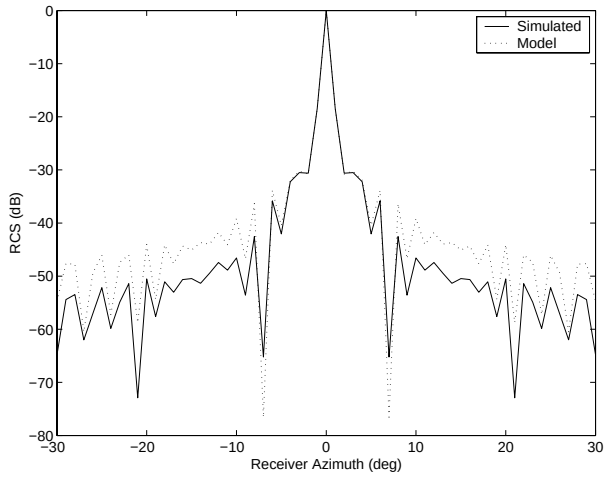

Figure 9. RCS of a dihedral as a function of receiver azimuth angle. The transmitter aspect angles are $(\phi_t, \theta_t) = (0°, 10°)$.

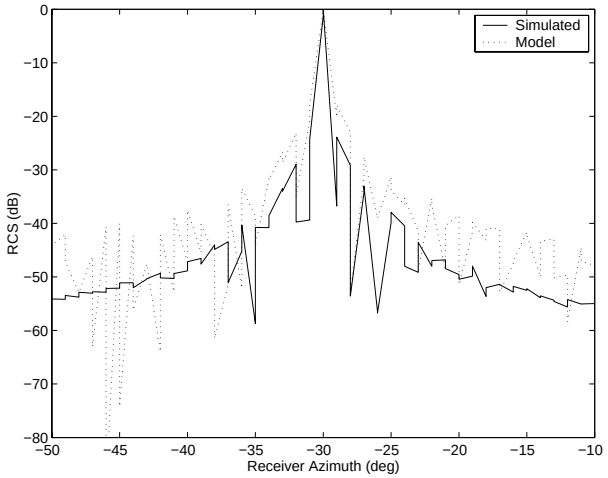

Figure 10. RCS of a dihedral as a function of receiver azimuth angle. The transmitter aspect angles are $(\phi_t, \theta_t) = (30°, 10°)$.

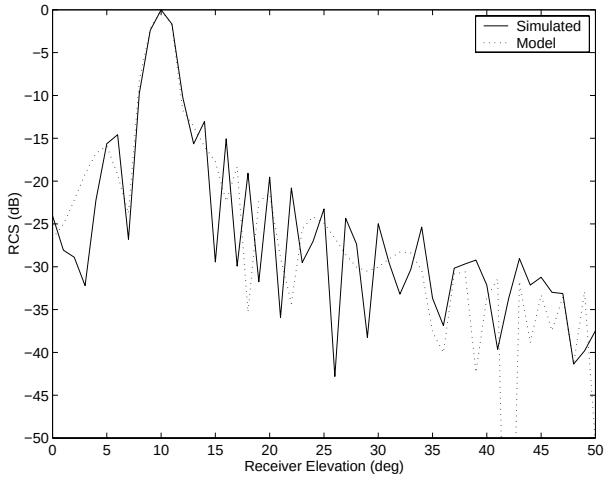

Figure 11. RCS of a dihedral as a function of receiver elevation angle. The transmitter aspect angles are $(\phi_t, \theta_t) = (0°, 10°)$.

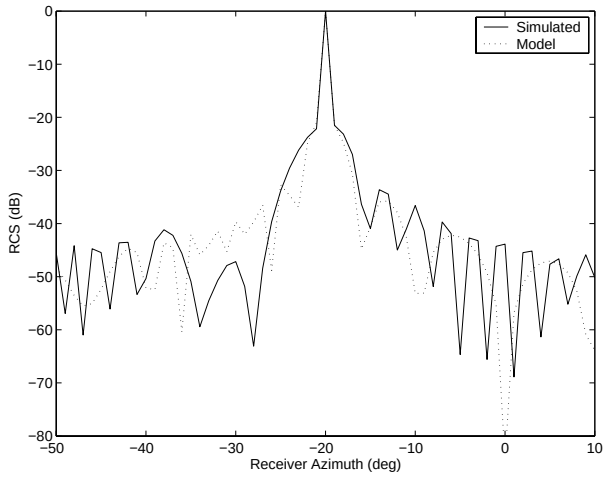

Figure 12. RCS of a clyinder as a function of receiver azimuth angle. The transmitter aspect angles are $(\phi_t, \theta_t) = (20°, 0°)$.

4.5. Cylinder

The bistatic response from a cylinder is modelled in azimuth as a flat scattering mechanism and in elevation as a circular mechanism. Thus, we write our scattering model for a cylinder as

$$\begin{aligned} S_{cyl}(f, \phi_t, \phi_r, \theta_t, \theta_r; L_m) &= S_{flat}(f, \phi_t, \phi_r; L_m, \phi_m = 0) S_{circ}(f, \theta_t, \theta_r) \\ &= \left(j \frac{f}{f_c}\right)^{1/2} \operatorname{sinc}\left(\frac{\pi f}{c} L_m (\sin\phi_t \cos\theta_t + \sin\phi_r \cos\theta_r)\right) \end{aligned}$$

$$\phi_t, \phi_r \in \left[-\frac{\pi}{2}, \frac{\pi}{2}\right] \tag{25}$$

where L_m is the length of the cylinder.

Figure 12 compares the Xpatchf simulated RCS of a cylinder to the modelled RCS, at $f = 10$ GHz. The cylinder has length $L_m = 4$ meters and radius 1 meter. The transmitter aspect is $(\phi_t, \theta_t) = (20°, 0°)$. The receiver azimuth angle varies from $\phi_r = -90°$ to $\phi_r = 90°$. Equation (25) accurately places the specular response from the cylinder at $-20°$ azimuth, and the principal side lobe behavior is matched reasonably well.

4.6. Plate

The plate scattering primitive is composed of flat scattering mechanisms in azimuth and in elevation. We therefore model its response as

$$\begin{aligned} S_{plate}(f, \phi_t, \phi_r, \theta_t, \theta_r; L_m, h_m) &= S_{flat}(f, \phi_t, \phi_r; L_m, \phi_m = 0) S_{flat}(f, \theta_t, \theta_r; h_m, \theta_m = 0) \\ &= \left(j\frac{f}{f_c}\right) \cdot \mathrm{sinc}\left(\frac{\pi f}{c} L_m(\sin\phi_t \cos\theta_t + \sin\phi_r \cos\theta_r)\right) \cdot \\ &\quad \mathrm{sinc}\left(\frac{\pi f}{c} h_m(\sin\theta_t + \sin\theta_r)\right) \\ &\quad \phi_t, \phi_r \in \left[-\frac{\pi}{2}, \frac{\pi}{2}\right], \quad \theta_t, \theta_r \in \left[-\frac{\pi}{2}, \frac{\pi}{2}\right] \end{aligned} \tag{26}$$

where L_m and h_m are the dimensions of the plate in azimuth and elevation, respectively. Note that the $\cos\theta_t$ and $\cos\theta_r$ terms are needed in the first $\mathrm{sinc}(\cdot)$ function, due to the aforementioned convergence of lines of longitude, but $\cos\phi_t$ and $\cos\phi_r$ terms are not needed in the second $\mathrm{sinc}(\cdot)$ function.

Figures 13 and 14 compare the Xpatchf simulated RCS of a flat plate to the modelled RCS, at 9 GHz. The plate has width $L_m = 2$ meters and has height $h_m = 2$ meters. The transmitter aspect angles are $(\phi_t, \theta_t) = (0°, 10°)$. The receiver azimuth angle varies from $\phi_r = -90°$ to $\phi_r = 90°$ in Figure 13, and the receiver elevation angle varies from $\theta_r = -90°$ to $\theta_r = 90°$ in Figure 14. Equation (26) matches the simulated RCS very well in both azimuth and elevation. Figure 14 shows a slightly worse match because, as with the earlier examples, the flat scattering mechanism model breaks down as the transmitter and receiver aspect angles separate and move away from broadside.

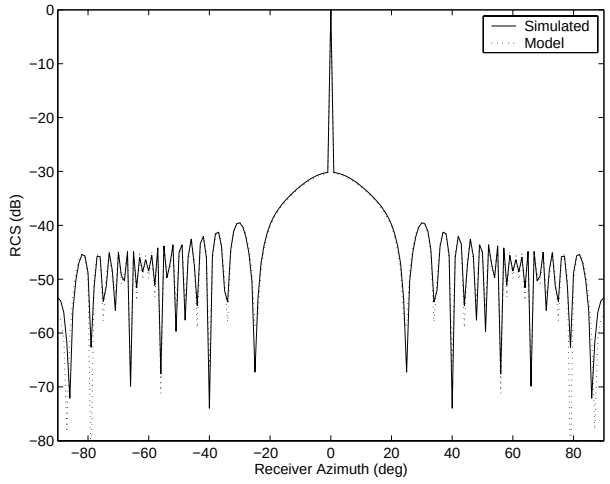

Figure 13. RCS of a flat plate as a function of receiver azimuth angle. The transmitter aspect angles are $(\phi_t, \theta_t) = (0°, 10°)$.

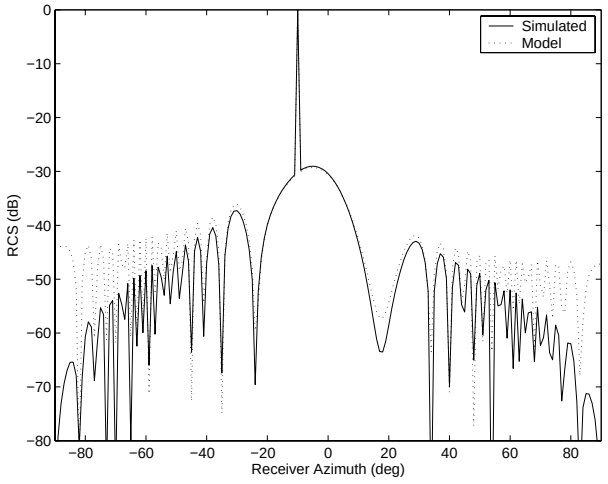

Figure 14. RCS of a flat plate as a function of receiver elevation angle. The transmitter aspect angles are $(\phi_t, \theta_t) = (0°, 10°)$.

4.7. Rotated Scattering Mechanisms

To obtain the response for a scattering mechanism that has undergone rotation transformations, one must apply the opposite rotations to the transmitter and receiver position vectors, to obtain the platform aspects in the object's rotated coordinate system. The resulting transmitter and receiver look angles, $(\hat{\phi}_t, \hat{\theta}_t)$ and $(\hat{\phi}_r, \hat{\theta}_r)$, may then be input to the model equations of the previous subsections. If a scattering center has roll γ, pitch β, and yaw α, its rotation transformation is given by

$$R(\alpha,\beta,\gamma) = \begin{bmatrix} \cos\alpha & -\sin\alpha & 0 \\ \sin\alpha & \cos\alpha & 0 \\ 0 & 0 & 1 \end{bmatrix} \begin{bmatrix} \cos\beta & 0 & \sin\beta \\ 0 & 1 & 0 \\ -\sin\beta & 0 & \cos\beta \end{bmatrix} \begin{bmatrix} 1 & 0 & 0 \\ 0 & \cos\gamma & -\sin\gamma \\ 0 & \sin\gamma & \cos\gamma \end{bmatrix}. \tag{27}$$

Thus, if the transmitting platform has aspect (ϕ_t, θ_t), its coordinates with respect to the rotated object are then given by

$$\begin{bmatrix} \hat{x}_t \\ \hat{y}_t \\ \hat{z}_t \end{bmatrix} = R(-\alpha,-\beta,-\gamma) \begin{bmatrix} \cos\phi_t \cos\theta_t \\ \sin\phi_t \cos\theta_t \\ \sin\theta_t \end{bmatrix}. \tag{28}$$

One may then compute the relative transmitter azimuth and elevation angles as

$$\hat{\phi}_t = \arctan\left(\frac{\hat{y}_t}{\hat{x}_t}\right) \quad \text{and} \quad \hat{\theta}_t = \arctan\left(\frac{\hat{z}_t}{\sqrt{\hat{x}_t^2 + \hat{y}_t^2}}\right). \tag{29}$$

The rotated receiver aspect angles $(\hat{\phi}_r, \hat{\theta}_r)$ are found analogously. The response of the rotated scatterer is obtained from $S_{\Gamma(m)}(f, \phi_t, \phi_r, \theta_t, \theta_r; \underline{\theta}^{(m)})$.

5. CONCLUSIONS

This paper introduced GTD-based models for bistatic scattering from canonical scattering centers. We presented three fundamental mechanisms for scattering in a plane: circular, flat, and right angle. These mechanisms were combined to form high-frequency separable models for the bistatic 3-D response from six scattering primitives: sphere, tophat, trihedral, dihedral, cylinder, and flat plate. A coupled model would likely be more correct electromagnetically in many cases, but based on comparisons of our proposed models to simulated RCS curves, the accuracy achieved is sufficient to allow one to estimate an object's physical parameters from a bistatic SAR image.

REFERENCES

1. O. Arikan and D.C. Munson, "A Tomographic Formulation of Bistatic Synthetic Aperture Radar," *Proc. ComCon '88* , p. 418, October 1988.
2. A.D.M. Garvin and M.R. Inggs, "Use of Synthetic Aperture and Stepped-Frequency Continuous Wave Processing to Obtain Radar Images," *South African Symposium on Communications and Signal Processing 1991* , pp. 32–35, 1991.
3. M. Soumekh, "Bistatic Synthetic Aperture Radar Inversion with Application in Dynamic Object Imaging," *IEEE Transactions on Signal Processing* **39**, pp. 2044–2055, September 1991.
4. N. Willis, *Bistatic Radar*, Technology Service Corporation, Silver Spring, MD, 1995.
5. C. Mikhail, K. Kurt, and N. David, "Bistatic synthetic aperture radar with non-cooperative LEOS based transmitter," *IEEE 2000 International Geoscience and Remote Sensing Symposium Proceedings* **2**, pp. 861–862, 2000.
6. J. Keller, "Geometrical theory of diffraction," *J. Opt. Soc. Amer.* , pp. 116–130, Jan 1962.
7. N. Tseng, "A very efficient rcs data compression and reconstruction technique," Master's thesis, Ohio State University, 1992.
8. L.C. Potter and R.L. Moses, "Attributed scattering centers for SAR ATR," *IEEE Transactions on Image Processing* **6**, pp. 79–91, January 1997.

9. L.C. Potter, D-M Chiang, R. Carriere, and M.J. Gerry, "A GTD-based parametric model for radar scattering," *IEEE Transactions on Antennas and Propagation* **43**, pp. 1058–1067, October 1995.
10. Z. Bi, J. Li, and Z. Liu, "Super resolution of SAR imaging via parametric spectral estimation methods," *IEEE Trans. Aerospace and Electronic Systems* **35**, pp. 267–281, January 1999.
11. M. Gerry, *Two-dimensional inverse scattering based on the GTD model*. PhD thesis, Ohio State University, 1997.
12. B. Rigling, "Physics, fisher and phase: Information content in sar images," Master's thesis, Ohio State University, 2000.
13. H. Chiang, R.L. Moses, and L.C. Potter, "Model-based classification of radar images," *IEEE Transactions on Information Theory* **46**, pp. 1842–1854, August 2000.
14. E. W. N.F. Chamberlain and F. Garber, "Radar target identification of aircraft using polarization-diverse features," *IEEE Transactions on Aerospace and Electronic Systems* **27**, pp. 58–67, Jan 1991.
15. D. Dudgeon and R. Mersereau, *Multidimensional Digital Signal Processing*, Prentice-Hall, Inc., Englewood Cliffs, NJ, 1984.
16. N. C. F.D. Garber and Ö. Snorrason, "Time-domain and frequency-domain feature selection for reliable radar target identification," *Proc. IEEE 1988 Nat. Radar Conf.* , pp. 79–84, Apr 1988.
17. S. et. al., "Validation of near-field monostatic to bistatic equivalence theorem," *IEEE IGARSS* **3**, pp. 1012–1014, 2000.
18. D.G.Falconer, "Near-field statement of monostatic-bistatic theorem," *Abstracts 1988 USRI National Radio Science Meeting* , Jan 1988.
19. J. Crispin and K. Siegel, *Methods of Radar Cross-Section Analysis*, Academic Press, New York, NY, 1968.
20. R.E.Kell, "On the derivation of bistatic RCS from monostatic measurements," *Proceedings of the IEEE* , pp. 983–988, Aug 1965.
21. E. A.-L.Germond and J.Saillard, "Foundations of bistatic radar and polarimetry theory," *IEE Radar Conference* , pp. 833–837, Oct 1997.
22. N. Akhter, *Far zone electromagnetic scattering from complex shapes using geometrical theory of diffraction*. PhD thesis, Ohio State University, 1993.
23. B.D. Rigling and R.L. Moses, "Motion Measurement Errors and Autofocus in Bistatic SAR," *To be submitted to IEEE Transactions on Image Processing* .
24. W.G. Carrara, R.S. Goodman, and R.M. Majewski, *Spotlight Synthetic Aperture Radar: Signal Processing Algorithms*, Artech House, Norwood, MA, 1995.
25. C.V. Jakowatz, D.E. Wahl, and P.H. Eichel, *Spotlight-Mode Synthetic Aperture Radar: A Signal Processing Approach*, Kluwer Academic Publishers, Boston, MA, 1996.
26. B.D. Rigling and R.L. Moses, "Polar Format Algorithm for Bistatic SAR," *Submitted to IEEE Transactions on Aerospace and Electronic Systems* , June 2002.
27. SAIC, *XPatch 4.6*, 2001.
28. P. E. J.Li, R.Wu and Z.Bi, "A robust hybrid spectral estimation algorithm for SAR imaging," *Signals, Systems & Computers, 1998. Conference Record of the Thirty-Second Asilomar Conference on* **2**, pp. 1322–1326, Nov 1998.
29. J. Z.Bi, K.Knaell and Z.-S.Liu, "Use of curvilinear SAR for three-dimensional target feature extraction," *Radar, Sonar and Navigation, IEE Proceedings* - **144**, pp. 275–283, Oct 1997.
30. E. G.Liu, J.Li and P.Stoica, "High-resolution SAR imaging with angular diversity," *IEEE Transactions on Aerospace and Electronic Systems* **37**, pp. 1359–1372, Oct 2001.